Automated techniques for the analysis of magnetic field inversion in filaments with the Solar Feature Catalogue

S. S. Ipson[a], V. V. Zharkova[a], S. Zharkov[a], A. K. Benkhalil[a], J. Aboudarham[b], N. Fuller[b]

[a] Department of Cybernetics, Bradford University, Bradford BD7 1DP, UK

[b] LESIA, The Paris-Meudon Observatory, F92195 Meudon Principal Cedex, FRANCE

Abstract

We present an automated comparison of magnetic-field inversion-line maps from SOHO/MDI magnetograms with solar filament data from the Solar Feature Catalogue created as part of the European Grid of Solar Observations project. The Euclidean distance transform and connected component labelling are used to identify nearest neighbour filament skeletons and inversion lines. Several filament-inversion line characteristics are defined and used to automate the decision whether a particular filament/inversion line pair is suitable for quantitative comparison of orientation and separation. The technique is tested on a total of 207 filaments from four Hα images, and the distributions of angles and distances between filament skeletons and LOS magnetic inversion lines are presented for 6 degrees of magnetic field smoothing. The results show the approach is robust and can be applied for a statistical analysis of magnetic field in filaments.

1. Introduction

Solar phenomena such as sunspots, filaments, flares and active regions vary with an 11 (22) year cycle, which is assumed to be connected with the behaviour of the solar magnetic field (Priest, 1984; Priest and Forbes, 2000). The solar magnetic field measured with the line-of-sight (LOS) ground-based or space-based magnetographs (Babcock and Babcock, 1955; Sherrer et al., 1995), or recent full vector magnetographs (Wang et al., 1998; Ulrich, 1992) provides an important data resource for understanding and predicting the solar activity. The importance of magnetic field has been emphasized in many theoretical works including: heating of the solar atmosphere; formation and support of multi-levelled magnetic loops and filaments resting on top of them; activation of energy releases in solar flares and coronal mass ejections; and in many other small and large scale events occurring in the solar atmosphere and interplanetary space.

It is supposed that different scales of magnetic field magnitudes account for solar events of different scales and that event scenarios result mostly from magnetic configurations of loops with opposite magnetic polarities (Priest and Forbes, 2000). For example, solar filaments often appear on the boundaries of coronal holes (Kuperus and Raadu, 1974; Lerche and Low, 1980) or above a middle line between two-ribbon flares (Sturrock and Jardin, 1994; Somov, 2000) that usually is very close to the location of magnetic inversion lines, or apparent magnetic neutral lines (AMNLs), later MNL.

This paper is concerned with attempting to analyse, fully automatically, data archived in the Solar Feature Catalogue generated by the European Grid of Solar Observations project (Zharkova et al., 2005), in order to identify relationships between magnetic field and solar phenomena; specifically between the line-of-sight magnetic inversion lines and solar filaments. It has long been accepted (Kippenhahn, Schluter, 1957; Lerche and Low, 1980) that filaments occur over inversion lines and over several decades a number of papers, including for example Duvall et al. (1977) and Durrant (2002), have presented superpositions of inversion line maps and filament maps and concluded there are favourable agreements on the basis of manual comparisons. In order to produce sufficient statistics for this comparison and to extract further information about the relationships an automated technique is required. The preparation and preliminary analysis of the magnetic field inversion maps is described in section 2.1 and the

methodology used to extract quantitative comparative information about the filaments and their neighbouring inversion lines is described in section 2.2. Some statistical results obtained from four days observations are then presented and discussed in section 3 and finally conclusions drawn in section 4.

2. Description of the techniques

Fig. 1 shows four examples of the superposition of automatically extracted filaments and magnetic inversion lines and illustrates the generally close association between filaments and inversion lines. However, the geometrical relationship between a filament and the nearest inversion line is not always simple. In order to develop algorithms to quantify this relationship we decided to use filament observations and magnetograms for the four dates indicated in the caption of Fig. 1. The filament data employed here were extracted from the Solar Feature catalogue and were automatically generated by Fuller et al. (2005), using H_α solar images from the Meudon Observatory. This data is defined on images standardised to a size of 1024×1024 pixel with a centred solar disk of radius 420 pixel.

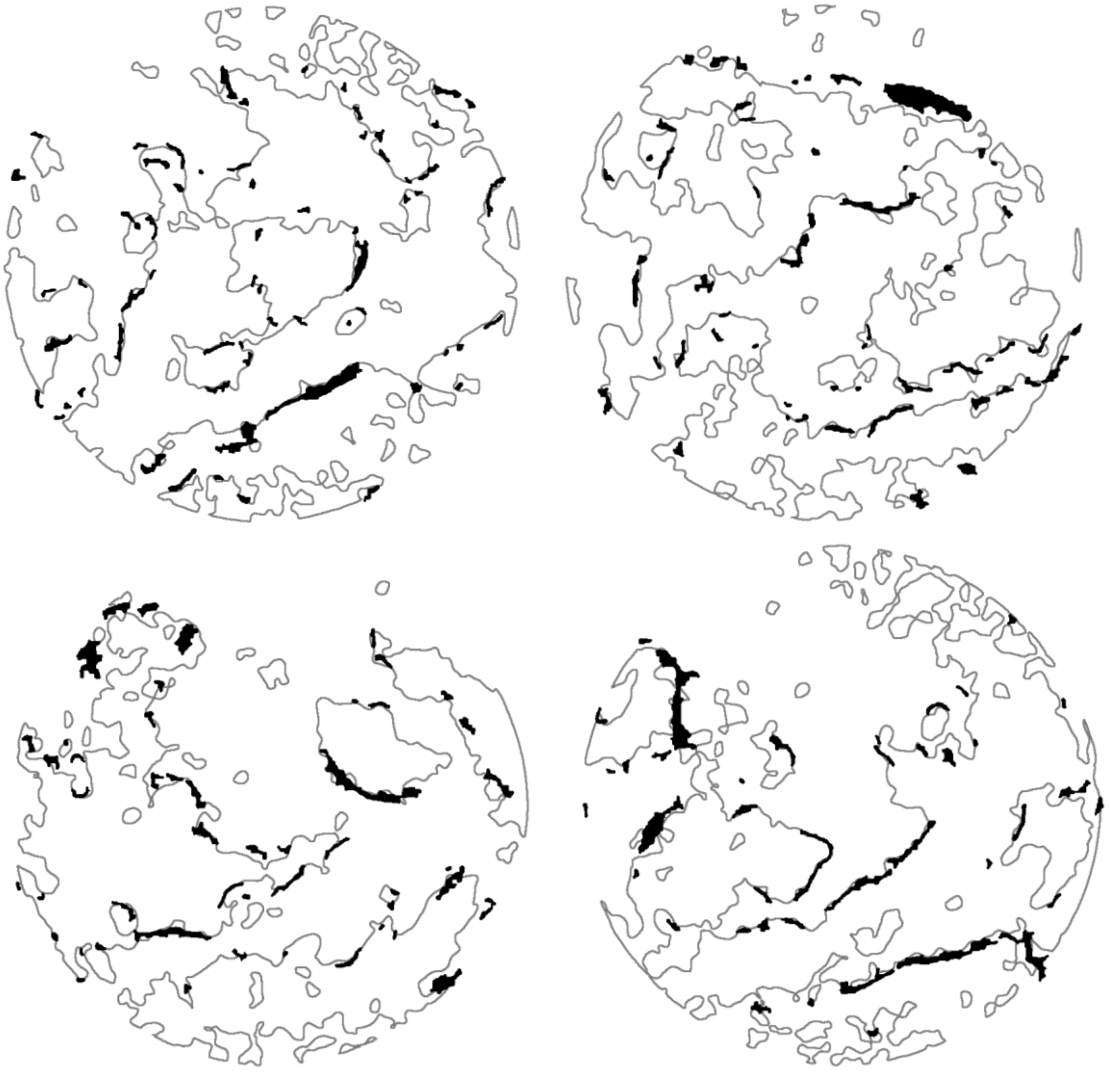

Fig. 1 Inversion line maps, clockwise from top left for 1 April, 9 April, 1 May and 5 July, 2002 computed using Gaussian convolution kernels with standard deviations of about 13″ (6 pixel) showing filament features from the Solar Feature Catalogue superimposed in black.

2.1. Preparation of magnetic field inversion maps

The sources of the magnetic data used in the comparisons are the four SOHO MDI line-of-sight (LOS) magnetograms which are closest in observation times to the H_α images. These magnetograms were synchronised to the H_α observation times and position and simultaneously remapped to the standardized size of the H_α images. The resulting magnetograms were then processed in the following way to produce inversion line maps for comparisons with the corresponding filament maps.

1. A 2-D Gaussian smoothing filter with kernel width equal to five times the standard deviation of the Gaussian distribution is applied.
2. Pixels in the smoothed magnetograms closest to points of magnetic field sign reversal are marked after checking for a change in sign in the horizontal, vertical and two 45° directions
3. The pixels marking inversion lines in step 2 may have more than two neighbouring points and to simplify the subsequent automatic interpretation of the inversion line data, the inversion point maps obtained in step 2 are thinned using the procedure due to Arcelli et al. (1981). The resulting inversion point maps now have most marked points falling on continuous lines with only two marked neighbours per point accept for a small number of crossovers, some of which are visible in Fig. 2.
4. As can be seen in Fig. 1, an inversion line map consists of a number of continuous lines of varying lengths and complexities. Fig. 2 illustrates the effect of increasing the amount of smoothing, which decreases the number of continuous lines and smoothes their shapes. As can be seen in Fig.2, the inversion line maps, particularly those with little smoothing, contain a significant number of inversion lines which we judged to be too small to be associated with filaments. Some of these (those 50 pixels or less in length) are eliminated at this stage as can be seen by comparing the comparable regions of Fig. 1 and Fig. 2. The determination of the lengths of the individual inversion lines is achieved by applying connected component labelling (Haralick and Shapiro, 1992) to the inversion maps obtained in step 3. This assigns the pixels on separate continuous inversion line different values and this is also used at the analysis stage to check whether or not two points are on the same inversion line.

Fig. 2 The right hand half of five inversion line maps with different amounts of smoothing computed, from left to right, using Gaussian kernels with standard deviations of about 9″,13″, 18″, 22″, and 30″ from a SOHO MDI line-of-sight magnetogram on 01/04/2002.

2.2. The methodology for comparison of filaments and magnetic inversion lines

The comparison between the filaments and the magnetic field inversion lines was simplified by taking into account only three points on each filament, namely, the start middle and end points of the filament skeleton and then determining the corresponding nearest points on the magnetic field inversion line map as illustrated in Fig. 3. The nearest points are found by applying a Euclidean distance transform (EDT) to the inversion line map using the algorithm of Cuisenaire and Macq (1999).

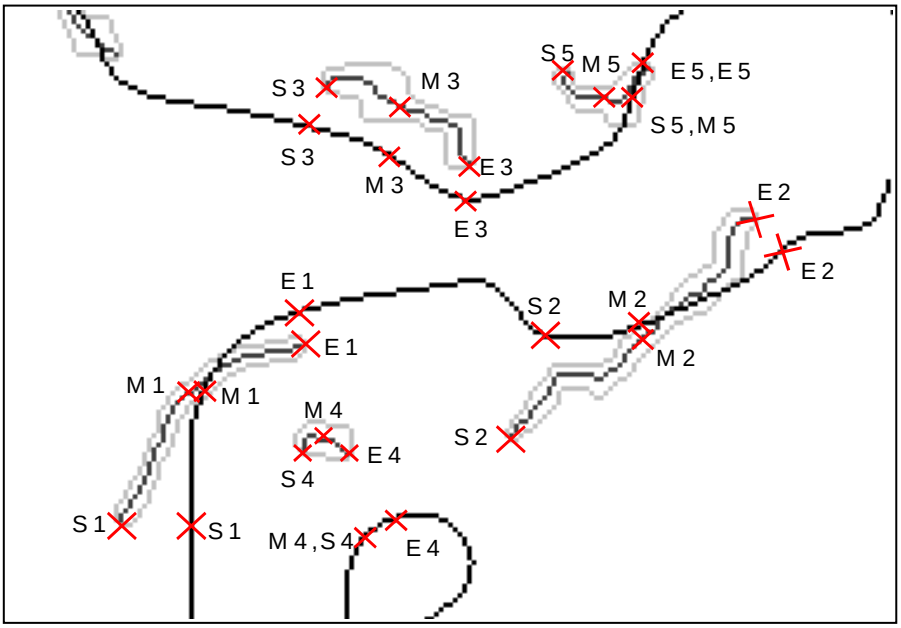

Fig. 3 Magnified region from the image dated 05/07/2002 in Fig.1 showing the three filament and corresponding inversion line pairs of points, labelled S, M and E associated with filaments numbered 1 to 5.

The mean of the three distances between the points on the filament and the nearest neutral line points is used as a measure of the filament to inversion line separation. The angle between the straight lines joining end points of a filament and the end points on the corresponding inversion line is used as a measure of the alignment between the filament and the neutral line. Although this approach is simple, it yields an angle which on manual inspection appears sensible, even in cases where the filament is severely curved as illustrated in Fig. 4. However, there are also cases where manual inspection indicates a numerical comparison is meaningless and these cases have to be identified automatically.

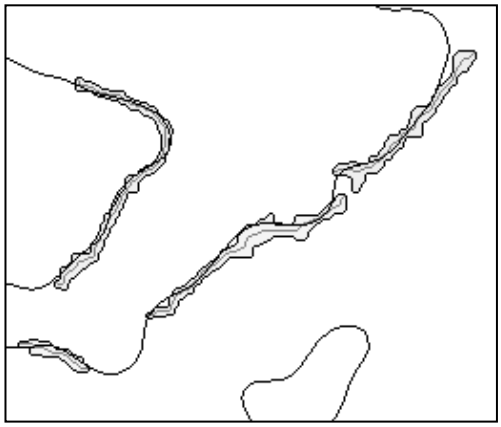

Fig. 4 Magnified region from the image dated 01/05/2002 in Fig. 1 showing four filament regions aligned at small angles with inversion lines

Five different situations have been identified from filament-inversion-line comparisons illustrated in Fig. 1 including smoothing standard deviations from 9″ to 30″ namely: i) the three inversion points associated with a filament are not all on the same inversion line; ii) the filament to inversion line distance is greater than the length of the filament; iii) the length of the inversion line segment associated with a filament is more than twice the length of the filament; iv) during tracking of the inversion line segment associated with a filament a point with only one or more than two neighbours was encountered; v) one or more of the three associated inversion line points are within half the width of the convolution kernel from the edge of the solar disk and are thus not correctly defined. The first four of these cases are illustrated in Fig. 5.

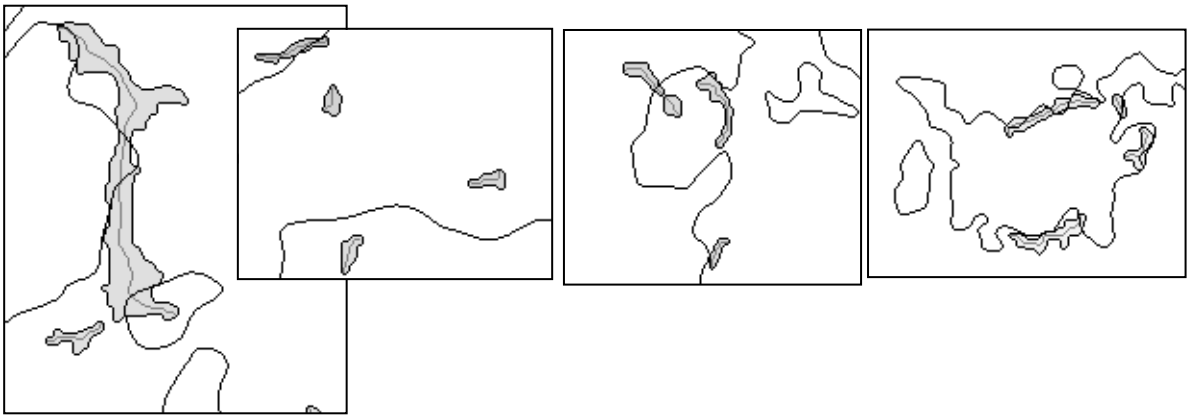

Fig. 5 Image fragments showing examples of filament and inversion line relationships i) to iv) described in the text from left to right. Cases i), ii) and iii) have 22″ smoothing and case iv) has 9″ smoothing.

3. The Results and Discussion

Comparisons of the data extracted from the Solar Feature Catalogue with SOHO MDI magnetogram data are presented in Figs. 6 - 14 for 207 filaments observed on 01/04/02, 09/04/02, 01/05/02 and 05/07/02 in H_α images from the Meudon observatory for magnetic field smoothing with standard deviations from about 9″ to 30″ (half widths ranging from 10 to 35 pixel). Fig. 6 shows the histograms of angles between the filament skeletons (axis) taken from SFC and the magnetic inversion lines. Histograms of distances between filament skeletons and inversion lines are presented in Figs. 7, 8 and 9 and distributions of LOS magnetic fields at filaments are presented in Figs. 10 and 11. Figs. 12, 13 and 14 show the data in Figs. 6, 7 and 11 divided into four bands of latitude of width 30°.

Only the filaments, which are not rejected by the criteria listed in section 2.2 are included in these Figs. The number of rejected filaments varies between 88 and 60 over the smoothing applied. Six of these rejected filaments are small and have large magnetic field intensities and are likely to be sunspots that are misclassified as filaments. It is also possible that some of the smaller features detected as filaments by Fuller et al. (2005) are fibrils/spicules, precondensations or filament barbs that are not distinguished by the static filament detection technique. Hence for reliable interpretation of such data in the future we need to introduce a feature tracking method that will allow us to investigate the filament dynamics and track precondensations and eliminate the features which do not belong to filaments.

The distribution of angles (Fig. 6) for all smoothing kernels is largest at 0º, falling towards zero with a half width about 15°. There is a secondary small broad peak centred at about 60° and manual inspection of the filament data shows that this is associated with small elongated features making large angles to the associated neutral line. The main peak in distribution for unsmoothed magnetic field is rather similar to the result obtained manually by Leroy (1978) for the distribution of angles between the long axis of prominences and a horizontal magnetic field measured with the full magnetic field vector for 16 prominences type A. In the present study we measure a LOS magnetic field; in most case it is a vertical component that is different from prominences. A similar outcome with the results by Leroy (1978) confirms, first, that the automated technique for their co-alignment reported above is robust and, second, filaments are most likely to be directed along a separator on the photosphere, or MNL (Priest and Forbes, 2000).

However, there is some evidence for the main peak narrowing and the secondary peak increasing in amplitude with the increase of magnetic smoothing (Fig. 2). This former result, i.e. closer elongation of MNLs along the filament skeletons is likely to point out that the increasing magnetic smoothing produces the inversion lines corresponding to higher altitudes in the solar atmosphere that better match to filament locations above the photosphere (Durrant, 2003). The latter result, i.e. a secondary peak in the angles, needs to be checked on more statistics since the number of filaments is very small. However, if it is correct then it suggests that with the increasing altitude there is a small increase in number of filaments making large angles with the inversion line that possibly can be flagging a magnetic configuration misbalance and needs to be investigated with both more observations to have a reliable statistics and theoretical models (Priest and Forbes, 2000)

Distributions of the MNL distances from the filament skeletons (Fig. 7) display single peaks, which have maxima at about 7″ and full widths at half maxima of about 14″ falling to lower magnitudes at about 40″. This can be a reflection either of an inclination of magnetic loops on the top of which the filaments are located (Demoulin and Priest, 1993; Priest and Forbes, 2000) or of magnetic field non-potentiality, or its helicity, that is reflected in a shift of a vertical magnetic field component observed in the current comparison.

If increasing magnetic smoothing effectively decreases the heights of filaments above the estimated inversion lines, so one can expect a decrease in the distance for filaments sitting directly above the inversion lines. However, it appears in Fig. 7 that the numbers of filaments with the smallest distance, on the contrary, decreases with the increase of magnetic smoothing and with increased smoothing the width of the peak appears to increase as well. This can be accounted for by the increasing helicity of magnetic lines (larger loop cross-sections), while approaching higher altitudes in the solar atmosphere. Alternatively, the expected effect may be masked by the variable statistics for the filaments that was mentioned in the second paragraph of this section.

To further examine the distribution of MNL distances from the filament skeletons, plots are shown in Figs. 8 and 9 of the signed distance from neutral line to filament skeleton. The sign is positive when a filament is further from the disk centre than the MNL. The signed distances from MNLs to filaments shown in Fig. 8 display a marked asymmetry, with positive distances two to three times more likely than negative distances. Fig. 9 displays separately signed distances for filaments inside and outside a circle of radius 30° from the disk centre comprising 25% and 75% respectively of the total disk area. Despite the poorer statistics for the smaller inner region, it appears that the asymmetry is associated with increasing distance of filaments from the centre and therefore is likely to be a projection effect on which is superimposed the same variation with smoothing seen in Fig.7.

The distributions of line-of-sight magnetic field within the filament and non-filament regions of the four solar observations considered are shown in Fig. 10. As expected filament

pixels are more likely to have smaller fields than non-filament pixels (in the ratio 1.5 to 2.3 (for SD 9″ to 30″) for the data in Fig. 10). The distributions for filament regions vary little with smoothing and are slightly asymmetric about zero field, whereas the distributions over the non-filament vary with smoothing and are more symmetric. This variation with smoothing accompanies the decrease in total length of the MNLs with increasing smoothing.

The histograms of line-of-sight magnetic fields at the three points on the filament skeletons (Fig. 11) display single peaks with maxima at zero and full widths of about 8 G. For the current observations in 2002 the peak is clearly asymmetric and filaments with the fields of -4 G are about twice as numerous as the filaments with fields of +4 G. This is in some agreement with the measurements by Leroy of the distribution of the magnetic field intensity in prominences, which was found to peak about 3.5 G (Leroy, 1977). The current distribution in Fig. 11 falls to a minimum at about ±15 G that is a sensitivity limit for MDI magnetic measurements (Scherrer et al., 1995). There is also some evidence that the number of filaments in the distribution peak around zero magnitude and increases with the increased magnetic smoothing (compare the different curves in Fig. 11). This is consistent with fact that by applying the increasing magnetic smoothing one estimates the inversion lines at higher altitudes in the solar atmosphere, giving better agreement with filaments (Durrant, 2003).

The results shown in Figs. 6, 7 and 11 have been also used for the distributions for four bands of heliographic latitude presented in Figs. 12, 13 and 14, respectively. The total numbers of filaments are about 15 in the band of 30° to 90°, about 45 in the 0° to +30° band, about 60 in the 0° to -30° band, and about 25 in the -30° to -90° band. From a comparison of Figs. 6, 7 and 11 and Figs. 12, 13 and 14 it can be seen that the dispersion in these distributions is increased compared with those shown in Figs. 6, 7 and 11, due to the lower number of filaments. This variation in dispersion is particular evident in the comparisons between latitude bands 30° to 90° and -30° to 0° because of the factor of four difference in numbers of filaments in these two bands. Despite the increased dispersion, some preliminary conclusions can still be drawn.

For instance, the distributions are asymmetrical at all latitudes, and this asymmetry is greater in the two equatorial bands, particularly the 0º to -30º band, than in the two polar bands. The equatorial magnetic distributions are also more than twice as wide as the polar distributions. In the latitude band from 0º to -30º the magnetic field distributions peak at 0G in all cases but the one with the largest smoothing. These results emphasize that there are some latitudinal and, possibly, longitudinal variations in filament magnetic fields, which are connected to the activity centres on a solar surface which are to be checked in the future on more reliable filament statistics for different phases of the solar cycle.

4. Conclusions

In the current paper we present some preliminary results of an automated comparison of solar filament elongations extracted from the Solar Feature Catalogues and LOS magnetic inversion lines detected using the software tools written in Microsoft C. The technique was tested on four Hα images from the Meudon Observatory populated into Solar Feature Catalogues, from which the data for 207 filaments have been automatically identified. The presented distributions have been automatically obtained, for first time as far as we are aware, for measures of filament to inversion line separation, filament to inversion line angle and filament magnetic field intensities and for different degrees of magnetic smoothing with standard deviations ranging from about 9″ to 30″.

For all smoothing kernels the distributions of angles between filament skeletons and MNLs (Fig. 6) is largest at 0º, falling towards zero with a half width about 15°. There is a secondary

small broad peak centred at about 60°. There is some evidence for the main peak narrowing and the secondary peak increasing in amplitude with the increase of magnetic smoothing.

The distributions of MNL distances from the filament skeletons (Fig. 7) display single peaks, which have a maximum at about 7″ and full widths at half maxima of about 14″ falling to lower magnitudes at about 40″. The numbers of filaments with the smallest distance decreases with the increase of magnetic smoothing and with increased smoothing the width of the peak appears to increase as well.

The distributions of line-of-sight magnetic fields (Fig. 11) display single peaks with maxima at zero and full widths of about 8 G. For the current observations in 2002 the peak is clearly asymmetric and filaments with the fields of -4 G are about twice as numerous as the filaments with fields of +4 G.

The distributions are asymmetrical at all latitudes, and this asymmetry is greater in the two equatorial bands, particularly the 0º to -30º band, than in the two polar bands. The equatorial magnetic distributions are also more than twice as wide as the polar distributions. In the latitude band from 0º to -30º the magnetic field distributions peak at 0G in all cases but the one with the largest smoothing.

We are aware that, because only 207 filaments are included in the current test research, it is difficult to identify the clear trends in the reported filament characteristics with the increased smoothing. However, in future research, we intend to apply this procedures to much larger numbers of such observations in order to improve the statistics and to ensure a sufficient reliability of the established and, possibly, new relationships with the new type of data. It has also to be noted that the detection technique used by the source of the filament data recognises some smaller features as filaments while they might in fact be fibrils/spicules, precondensations or filament barbs. Hence in the future we need to introduce a feature tracking method that will allow us to investigate filament dynamics (and track precondensations) to eliminate features which do not belong to filaments and to join broken filament segments together.

Acknowledgements

The authors would like to thank the referees for their helpful comments which have significantly improved the paper. The work has been supported under project IST-2001-32409 by the European Commission within the Information Society Technologies thematic priority of the Fifth Framework Program.

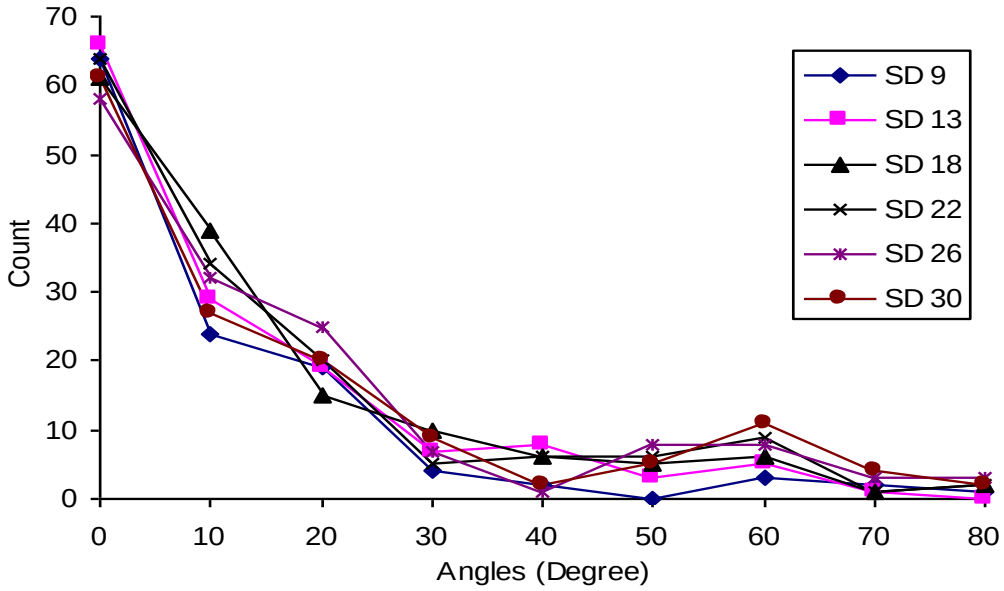

Fig. 6 Histograms of angles between filaments and neutral lines for smoothing kernels with standard deviations of 9″ to 30″ (half widths 10 to 35 pixel in steps of 5 pixel).

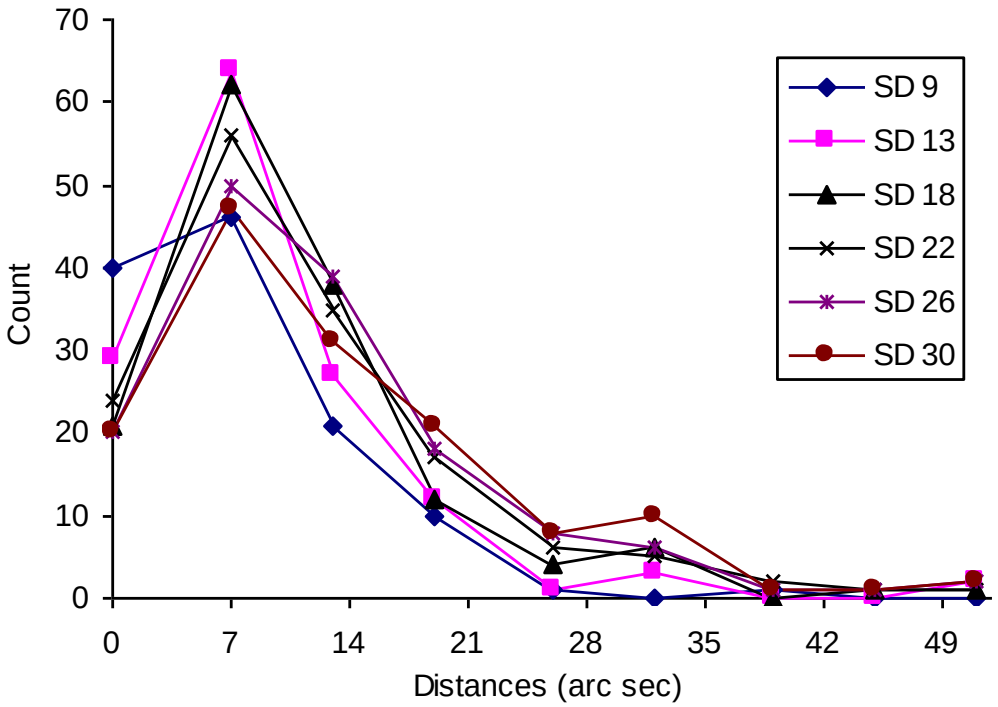

Fig. 7 Histograms of distances in arc sec between filaments and neutral lines for smoothing kernels with standard deviations of 9″ to 30″ (half widths 10 to 35 pixel in steps of 5 pixel).

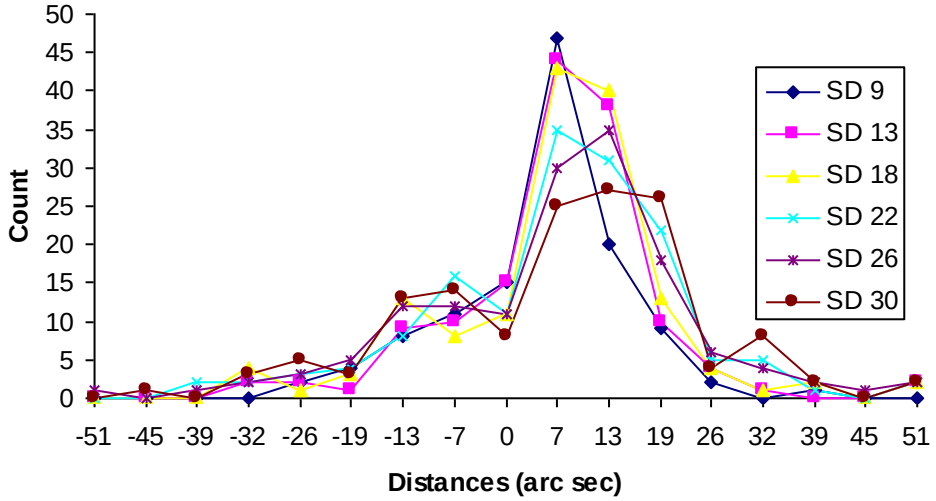

Fig. 8 Histograms of signed distances in arc sec from neutral lines to filaments for smoothing kernels with standard deviations of 9″ to 30″ (half widths 10 to 35 pixel in steps of 5 pixel).

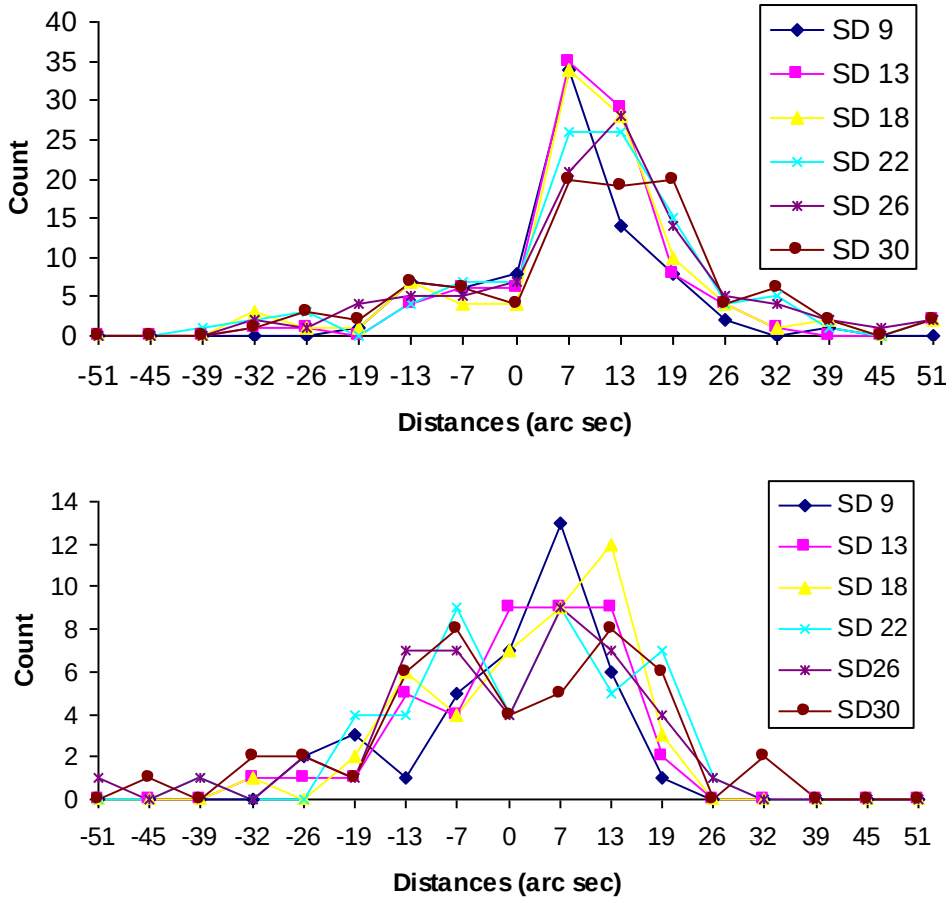

Fig. 9 Histograms of signed distances in arc sec from neutral lines to filaments for filaments greater than 30° from disk centre at top and less than 30° from disk centre at bottom, for smoothing kernels with standard deviations of 9″ to 30″ (half widths 10 to 35 pixel in steps of 5 pixel).

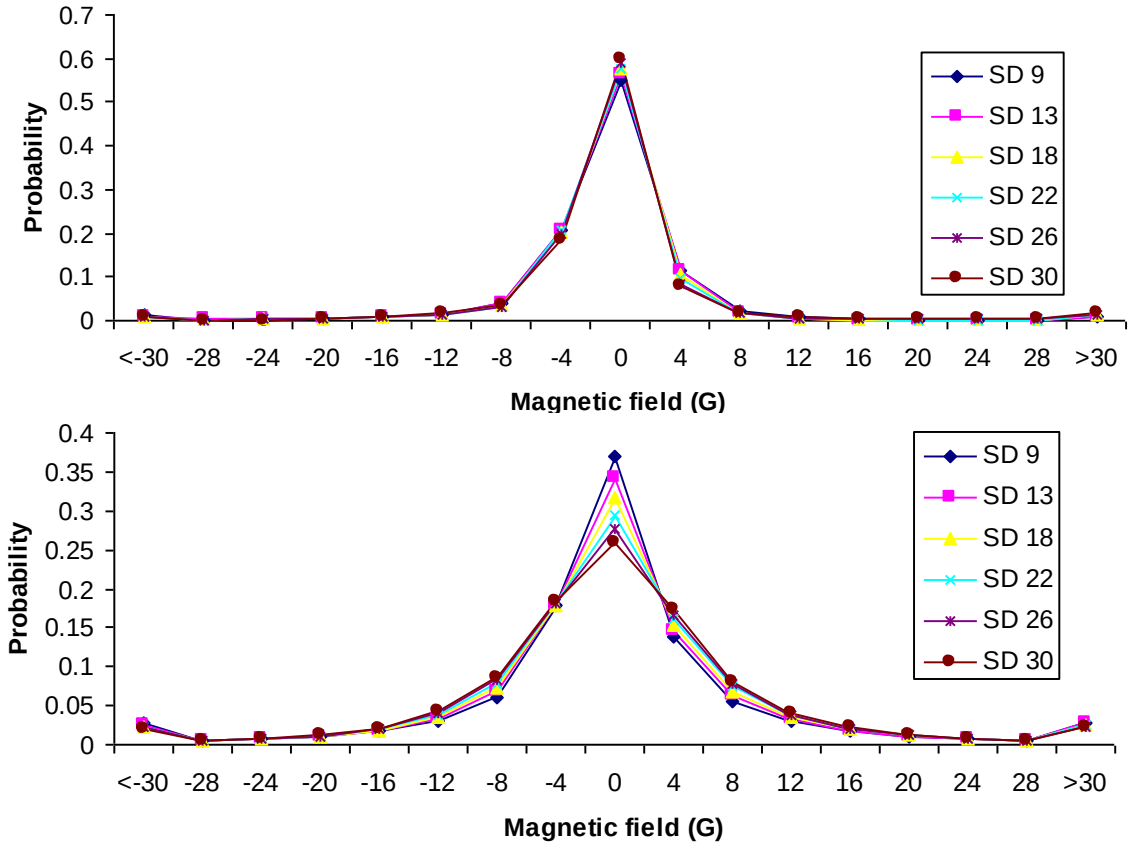

Fig.10 Distributions of line-of-sight magnetic field over the filament regions of the four magnetograms at top and over non-filament regions at bottom, for smoothing kernels with standard deviations of 9″ to 30″ (half widths 10 to 35 pixel in steps of 5 pixel).

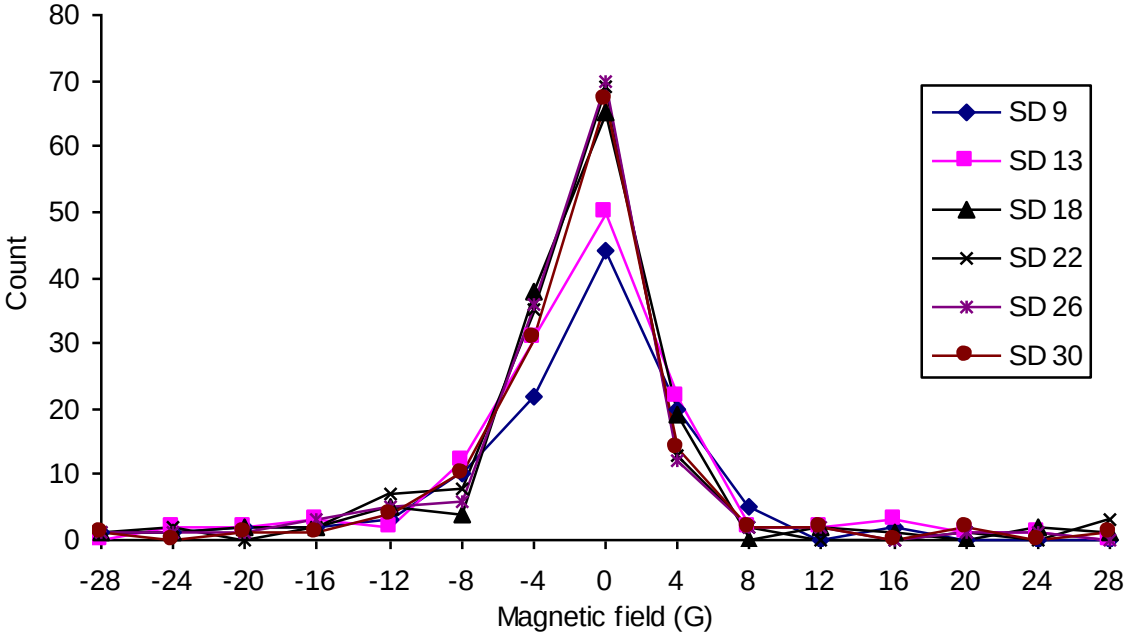

Fig. 11 Histograms of line-of-sight magnetic field in Gauss for smoothing kernels with standard deviations of 9″ to 30″ (half widths 10 to 35 pixel in steps of 5 pixel)

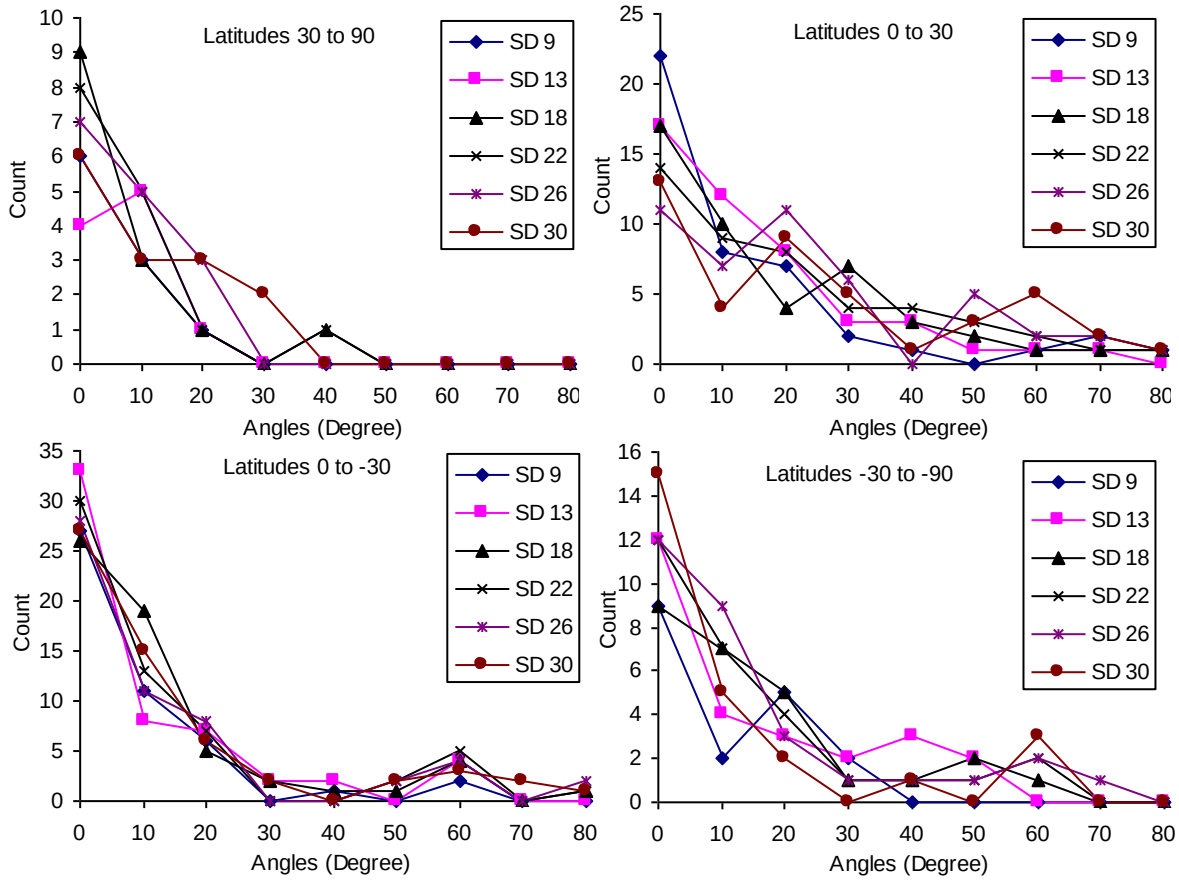

Fig. 12 Histograms of filament to inversion line angle separated into four bands of latitude for smoothing kernels with standard deviations of 9″ to 30″ (half widths 10 to 35 pixel in steps of 5 pixel).

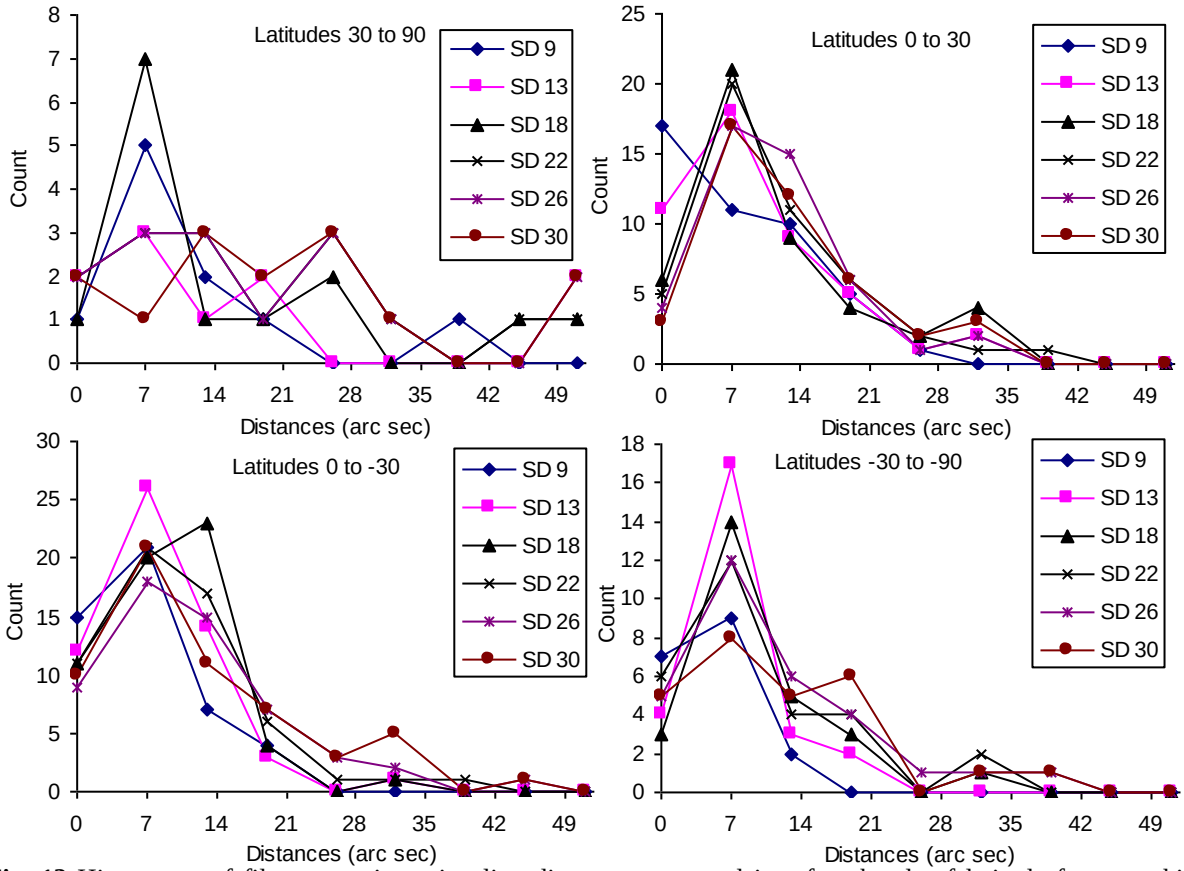

Fig. 13 Histograms of filament to inversion line distances separated into four bands of latitude for smoothing kernels with standard deviations of 9″ to 30″ (half widths 10 to 35 pixel in steps of 5 pixel).

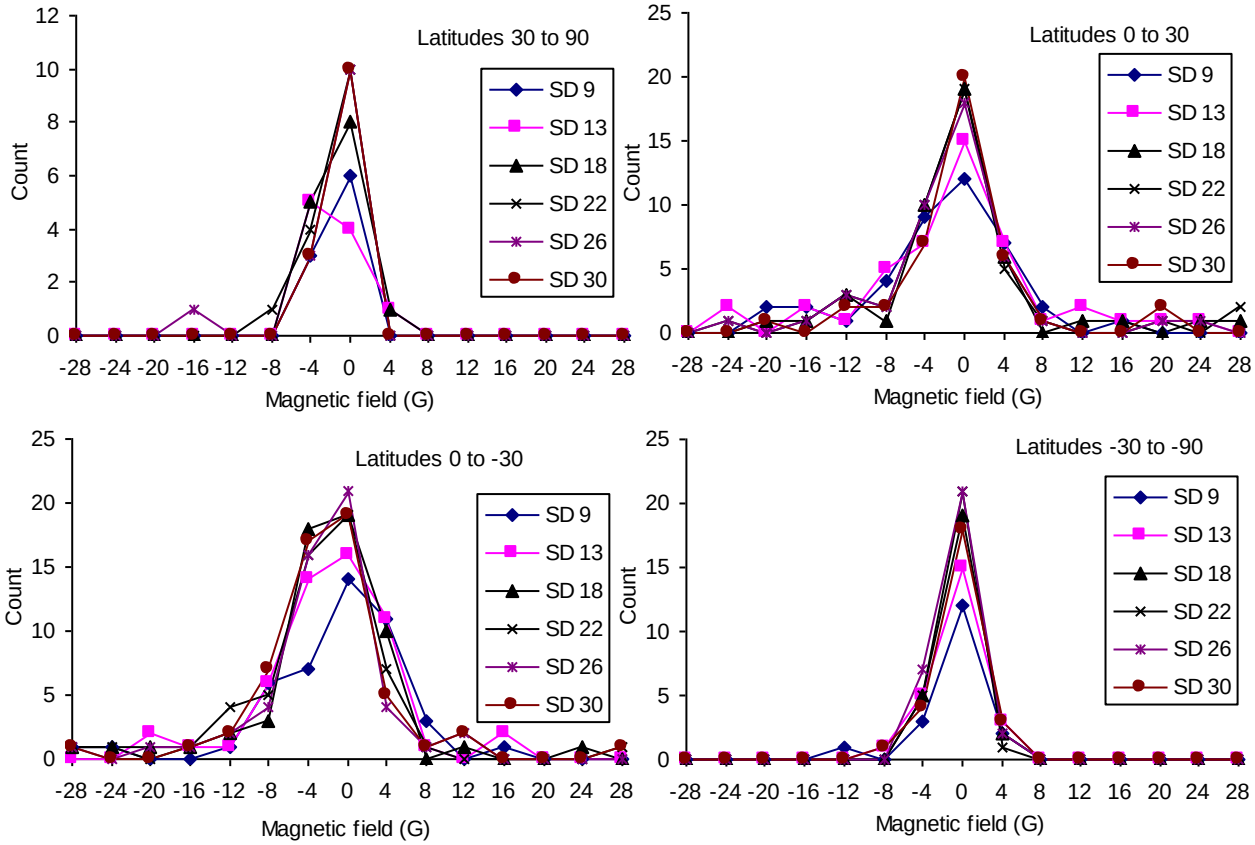

Fig. 14 Histograms of line-of-sight magnetic fields in Gauss at filaments separated into four bands of latitude for smoothing kernels with standard deviations of 9″ to 30″ (half widths 10 to 35 pixel in steps of 5 pixel).

References

Arcelli, C., Cordella, L. P., Levialdi, S. From local maxima to connected skeletons. IEEE Trans. Patt. Anal. Machine Intell., PAMI-3-2, 134-143, 1981.

Babcock, H. V., Babcock, H. D. The Sun's Magnetic Field, 1952-1954. Astrophysical Journal, 121, 349-366, 1955.

Cuisenaire, O. Macq, B. Fast and exact signed Euclidean distance transformation with linear complexity. In Proc. IEEE Int. Conference on Acoustics, Speech and Signal Processing (ICCASSP99), 6, 3293-3296, Phoenix (AZ), March 1999.

Demoulin, P., Priest, E.R. A model for an inverse-polarity prominence supported in a dip of a quadrupole region, Solar Physics, 144, 283-305, 1993.

Durrant, C. J. Polar magnetic fields-filaments and the zero-flux contour. Solar Physics, 211, 83-102, 2002.

Duvall, T. L., Wilcox, J. M., Svalgaard, L., Scherrer, P. H., McIntosh, P. S. Comparison of Hα synoptic charts with the large-scale solar magnetic field as observed at Stanford. Solar Physics, 55, 63-68, 1977.

Fuller, N., Aboudarham, J., Bentley, R. D. Filament recognition and image cleaning on Meudon H_α spectroheliograms. Solar Physics, 227, 61-73, 2005.

Haralick, R. M., Shapiro, L. G. Robotic Vision. 1, 28, Addison Wesley Publishing Company, 1992.

Kippenhahn, Schluter. Eine Theorie der solaren Filamente. Zeitschrift für Astrophysik,43, 36-62, 1957.
Kuperus, M., Raadu, M. A. The Support of Prominences Formed in Neutral Sheets. Astronomy and Astrophysics, 31, 189-193, 1974.
Lerche, I., Low, B. C. Cylindrical prominences and the magnetic influence of the photospheric boundary2. Solar Physics, 66, 285-303, 1980.
Leroy, J. L. On the intensity of magnetic field in quiescent prominences. Astron. Astrophys., 60, 79-84, 1977.
Leroy, J. L. On the orientation of magnetic fields in quiescent prominences. Astron. Astrophy., 64, 247-252, 1978.
Priest, E. R. Solar magneto-hydrodynamics. Geophysics and Astrophysical Monographs, Dordrecht: Reidel, 1984.
Priest, E. R., Forbes, T. Book Review: Magnetic reconnection. Cambridge U Press, 2000.
Scherrer, P. H. et al. Annual Review. Astr. Astrophys., 2, 363, 1995.
Somov, B.V. Cosmic Plasma Physics. Astrophysics and Space Science Library,252. Boston, Mass.:Kluwer Academic Publishing, 2000.
Sturrock, P.A., Jardin, M. Book Review: Plasma physics. Cambridge U Press, 1994.
Ulrich, R. K. In Cool Stars, Stellar Systems and the Sun. edited by M. S. Giampapa and J. A. Bookbinder, Astron. Soc. of the Pacific, San Francisco, Calif., 265, 1992.
Wang, H., Denker, C., Spirock, T., 7 other authors. New Digital Magnetograph At Big Bear Solar Observatory. Solar Physics, 183, 1-13, 1998.
Zharkova, V V., Aboudarham, J., Zharkov, S., Ipson, S.S., Benkhalil A.K., Fuller, N. Solar Feature Catalogues in EGSO, Solar Physics, 228, 139-152, 2005.